Supporting information

Ultra-High Piezoelectric Properties and Ultra-High Curie Temperature of Li/Ce Doping La$_2$Ti$_2$O$_7$ Ceramics

Manjing Tang, Zhi Tan,* Jie Xing, Hao Chen, Xinji Yang, Hongjiang Li, Wen Zhang, and Jianguo Zhu*

M. J. Tang, Z. Tan, J. Xing, H. Chen, X. J. Yang, H. J. Li, W. Zhang, J. G. Zhu
College of Materials Science and Engineering,
Sichuan University,
Chengdu 610064, China.
E-mail: tanzhi0838@scu.edu.cn, nic0400@scu.edu.cn

Theoretical Study of LTO Structure

1. Structural Properties

LTO is commonly considered undergoing three distinct solid phases with the change of temperature. Above 1773 K, the LTO is paraelectric *Cmcm* structure. With the decreased temperature, the rotation of the TiO$_6$ octahedra around the Ti atoms and the relative displacement of cations and anions break the mirror plane perpendicular to the *c* axis, emerging polar structure. In this phase transition process, the rotation of the TiO$_6$ octahedra (it is usually termed antiferrodistortive, AFD) is not be regarded as zero contribution for inducing ferroelectricity unlike those perovskite structure. Due to the unique layered structure, its perovskite block is truncated along *b* axis with *n* = 4, and holding 5 layered oxygens in the block. In this case, the AFD distortion will induce the displacement along *c* axis for each layered oxygen, generating *p*, *-p*, *p*, *-p*, and *p* local dipole along *b* direction. For the perovskite structure, corresponding to *n* = ∞, the *p* and *-p* are equally divided when the AFD occurs, and therefore no net polarization is residual. However, total dipole associated with one block would be *p* for LTO, which is detailed in López-Pérez work.[1] The temperature is further reduced to approximately 1053 K, the LTO transforms to *P*2$_1$ structure due to the anti-phase tilting of the TiO$_6$ octahedra along *a*-axis. The *P*2$_1$ structure is the room-temperature structure for LTO, and no other low-temperature phase have been reported until now. Table S1 shows the

calculated equilibrium ferroelectric structure of *Cmc2₁* and *P2₁* phases of LTO considered in this paper. All calculated results are consistent with the experimental structures. The total energy difference between $P2_1$ and $Cmc2_1$ structures is -100.1 meV/f.u., which is compatible with the experimental results and suggests the $Cmc2_1$ phase is high-temperature structure.

Table S1. The calculated equilibrium ferroelectric structure of *Cmc2₁* and *P2₁* phases of LTO.

$Cmc2_1$	$a = 3.896$ Å; $b = 25.427$ Å; $c = 5.520$ Å; $\alpha = \beta = \gamma = 90°$			
	$(a = 3.954$ Å; $b = 25.952$ Å; $c = 5.607$ Å; $\alpha = \beta = \gamma = 90°)^2$			
Atom	Wyc.	x	y	z
La(1)	4a	0.0000	0.2969	0.1627
La(2)	4a	0.0000	0.4471	0.7466
Ti(1)	4a	0.0000	0.8373	0.7051
Ti(2)	4a	0.0000	-0.0600	0.2405
O(1)	4a	0.0000	0.7802	-0.0790
O(2)	4a	0.0000	0.7968	0.4376
O(3)	4a	0.0000	0.8831	0.0490
O(4)	4a	0.0000	-0.0920	0.5598
O(5)	4a	0.0000	-0.0110	-0.0290
O(6)	4a	0.0000	0.3465	0.7452
O(7)	4a	0.0000	0.4509	0.2658
$P2_1$	$a = 7.744$ Å; $b = 5.514$ Å; $c = 13.010$ Å; $\alpha = \gamma = 90°$; $\beta = 98.602°$			
	$(a = 7.8$ Å; $b = 5.546$ Å; $c = 13.011$ Å; $\alpha = \gamma = 90°$; $\beta = 98.6°)^3$			
La(1)	2a	0.6498	0.2020	0.6117
La(2)	2a	0.1471	0.1516	0.5797
La(3)	2a	0.7205	0.7459	0.8840
La(4)	2a	0.2270	0.7389	-0.0968
Ti(1)	2a	-0.0762	0.7082	0.6783
Ti(2)	2a	0.4177	0.7030	0.6742
Ti(3)	2a	-0.0313	0.2335	0.8816
Ti(4)	2a	0.4728	0.2349	0.8797

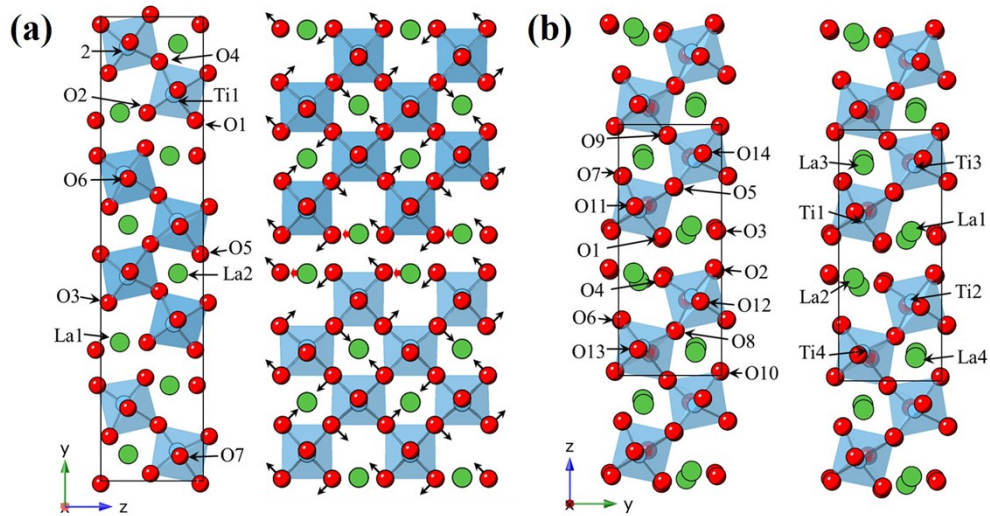|				
O(1)	2a	0.8769	-0.0719	0.5696
O(2)	2a	0.4042	-0.0830	0.5601
O(3)	2a	-0.0853	0.4445	0.5915
O(4)	2a	0.382	0.4273	0.6033
O(5)	2a	0.8924	0.0325	0.7734
O(6)	2a	0.4938	0.0391	0.7701
O(7)	2a	-0.0286	0.5451	0.8146
O(8)	2a	0.4375	0.5502	0.8161
O(9)	2a	-0.0343	-0.0249	-0.0172
O(10)	2a	0.5254	-0.0251	-0.0191
O(11)	2a	0.6725	0.6628	0.6916
O(12)	2a	0.1742	0.7883	0.6963
O(13)	2a	0.2233	0.1952	0.8923
O(14)	2a	0.7270	0.3107	-0.0923

Figure S1 (a) Crystal structure of $Cmc2_1$ and the schematic diagram of topological phase transition for inducing net polarization due to oxygen octahedron tilting; (b) crystal structure of $P2_1$.

2. Polarization Change from $Cmc2_1$ to $P2_1$ Transition

The previous reported first-principle calculations shows the extreme reduction of spontaneous polarization from $Cmc2_1$ to $P2_1$ transition using Berry-phase theory, which

shows 0.29 [1] and 0.0772 C/m² [4], respectively. Although it is generally believed that AFD and ferroelectric (FE) modes tend to compete and suppress each other in perovskite structures,[5] the significant reduction of polarization from $Cmc2_1$ to $P2_1$ transition in LTO is still incredible. Due to nature of Berry-phase method, the spontaneous polarization is defined as the difference in polarization of the ferroelectric structure and a suitable paraelectric or antiferroelectric reference structure via an adiabatic switching path. Hence, the calculated spontaneous polarization is strongly dependent on the choices of branch of polarization quanta with a right distortion pathway. It must be especially noted in the LTO supercell contained 44 atoms and inducing significantly large atomic distortions from $Cmcm$ to $Cmc2_1$ or $P2_1/m$ to $P2_1$ transition, which means the small quantum of polarization and is not easy to align individual atoms for seeking reasonable distortion pathway. We therefore carefully construct the distortion pathway adopted finding the minimum total distortion amplitude to ensure accuracy. First, we choose an atom as the reference point to match the lattice and decrease the global translation between two phases, such as one La2 atom in $Cmc2_1$ structure, where the distortion is smaller than other sites (Figure S1). Second, the atom of each element constructs the one-to-one correspondence, then using the follow equation to calculate the total distortion amplitude,

$$D_a = \sqrt{\sum_i \Delta X_i^2}$$

(1)

where ΔX is the difference of displacement between polar phase and reference phase. To decrease the computational cost, the atom of each element set a cut-off radius of 4 Å when finding the one-to-one correspondence. After completion, smallest total distortion amplitude between polar phase and reference phase indicates the reasonable distortion pathway. Early manual evaluation can be effectively decreases the computational number of times.

As shown in Figure S2(a) and (c), the polarization quantums are 0.161 and 0.162 C/m² for $P2_1$ and $Cmc2_1$ structures, respectively, calculated using $\Delta P = e\mathbf{R}/\Omega$, where e is the charge of the electron, $\mathbf{R}$ is the lattice vector in the direction of the polarization and Ω

is the unit cell volume. It should be noted that our adopted ferroelectric $P2_1$ and $Cmc2_1$ structures are polar along negative b and c directions, respectively. The Figure S2(a) and (c) definitely shows a continuous pathway to connect the original ferroelectric structure to the inverted ferroelectric structure via the centrosymmetric structure. Choosing any one branch of quantum, the spontaneous polarizations are calculated as -0.251 and -0.342 C/m^2 for $P2_1$ and $Cmc2_1$ structures, respectively. We found the polarization of $Cmc2_1$ structure is compatible with López-Pérez's work reported 0.29 C/m^2 [1], and the difference can be attributed to usage of different exchange-correlation functional, where the LDA usually underestimates the ferroelectric polarization[6]. However, the spontaneous polarization of $P2_1$ is significantly different with Bruyer's work reported 0.0772 C/m^2 [4]. Using the same exchange-correlation functional, our work confirms that the decrease of polarization from $Cmc2_1$ to $P2_1$ transition with the decline of temperature, but the descend range is not extremely significant as previous declaration. The $Cmc2_1$ phase is the high-temperature structure of LTO, hence, the result suggests that LTO has a positive pyroelectric coefficient when the temperature increases gradually from room temperature to the certain high temperature.
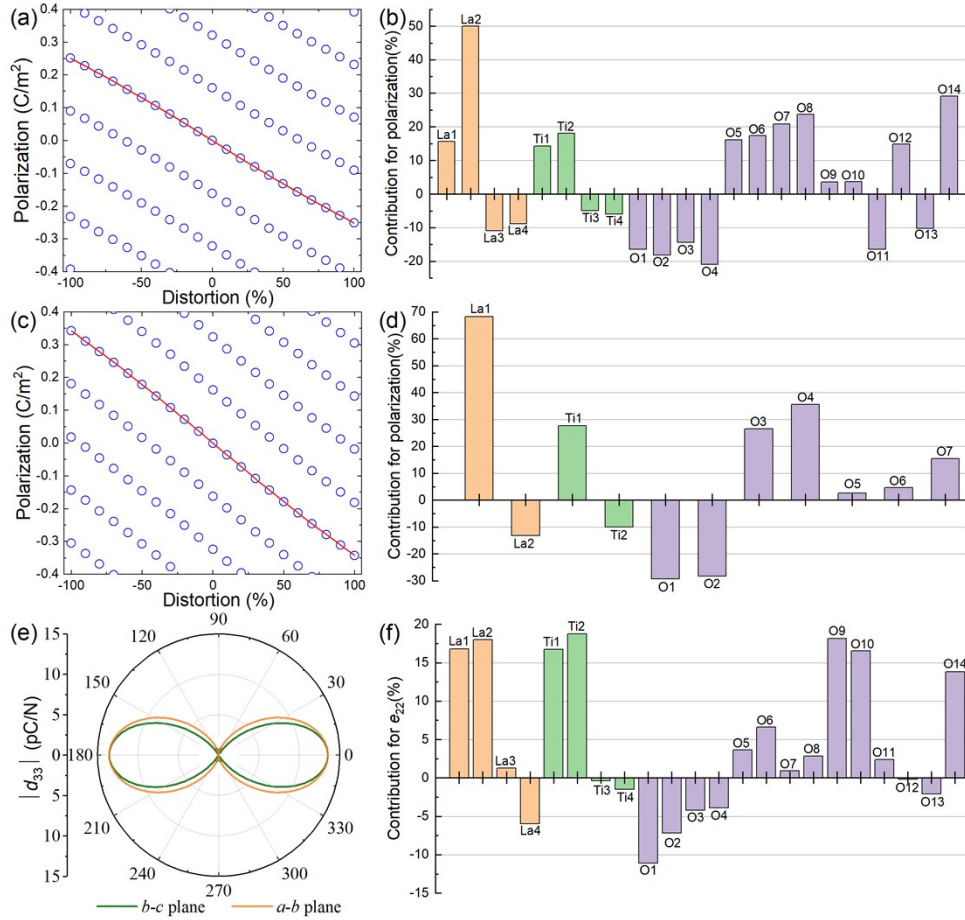
Figure S2 (a) Change in polarization along a distortion pathway from the original $P2_1$ structure through the centrosymmetric $P2_1/m$ structure to the inverted -$P2_1$ structure and (b) its individually atomic contribution for polarization in $P2_1$ structure. (c) Change in polarization along a distortion pathway from the original $Cmc2_1$ structure through the centrosymmetric $Cmcm$ structure to the inverted -$Cmc2_1$ structure and (d) its individually atomic contribution for polarization in $Cmc2_1$ structure. In which the small bule circles represent possible polarization values in different branch of polarization quanta to a certain distortion. (e) Orientation dependence of effective d_{33} in $P2_1$ structure, the degree denotes the angle from b-axis. (f) Individually atomic contribution for e_{22}.

The origin of ferroelectricity of $Cmc2_1$ structure is considered as O_6 octahedra rotations induced dominant FE instability in LTO.[1] However, the polarization is still dominated by a significant deformation of the O_6 octahedra and the displacements of O and La.[1] To study the polarization quantitatively, we use the approximate formula

$$P_\alpha = \frac{1}{\Omega} Z^*_{i,\alpha\beta} \Delta X_{i,\beta}$$

(2)

Where i labels the atoms in the unit cell, and α and β label spatial directions, Z^* is Born effective charge tensors, and ΔX is the change of displacement. We employ the convention of $\sum_i \Delta X_{I,\beta} = 0$ to eliminate the global atomic translation, then combining the equation (1), the total polarization can be decomposed into individually atomic contribution. Using their Born effective charge tensors, the total polarizations of $P2_1$ and $Cmc2_1$ structures can be obtained as -0.231 and -0.318 C/m^2, which are basically compatible with the results calculated from Berry-phase method.

The obtained individually atomic contributions for polarizations of $P2_1$ and $Cmc2_1$ structures are shown in Figure S2(b) and (d), respectively. The results agree López-Pérez's conclusion[1] that the polarization is still dominated by atomic displacement rather than the rotation of O_6 octahedra. More interesting, our results demonstrate that the rotation of O_6 octahedra have a negative contribution for the total polarization despite it is the origin of ferroelectricity in LTO. For simplicity, we consider the rotation of O_6 octahedra around x-axis in $Cmc2_1$, and 5 layers of rotated O atoms from the O_6 octahedra gap to the next gap can be found. It is can be found that the first and fifth layers are labeled by O1 and O2, the second and fourth layers are labeled by O3 and O4, and the third layer is labeled by O5. The rotation of O_6 octahedra give rise to the different direction of displacement for adjacent oxygen layers, which means the opposite contribution each other for total polarization, such as p, $-p$, p, $-p$, and p layered local dipole. Hence, this part polarization direction induced by pure rotation of O_6 octahedra should be consistent with the contributions of O1 and O2. However, both of O1 and O2 have a negative contribution for total polarization, suggesting that the relative displacement or deformation of O_6 octahedra is the major source of spontaneous polarization despite the rotation of O_6 octahedra has been considered as the origin of ferroelectric instability. We noted that the La2 and Ti2 follow the rotation of O_6 octahedra giving the negative contribution, whereas La1 and Ti1 give the strong positive contribution for spontaneous polarization. The difference is strongly dependent

on its layered structure. The La1 locates at the outermost layer of perovskite block and La2 locates at the inside of perovskite block. The La2 is stable around the center of 12-fold coordinated oxygen cage, which is very similar to A-site of the typical perovskite structure. For the La1, Coulomb force from the adjacent Ti makes it moving to the surface of perovskite block, and it is stable almost in the center of square constructed by O1 and O2. The rotation of O_6 octahedra makes the O1 and O2 displaced to the negative c direction, then the strongly short-range repulsion force enforces La1 move in the same direction. However, the force on the La2 almost cancel each other out due to the continuity of local perovskite cell. The large displacement of La1 also causes Ti1 to move towards the same direction due to long-rang Coulomb repulsion. Consequently, the La1 and Ti1 produce the massive contribution for the total polarization, while influence of La2 and Ti2 is limited. Based above analysis, it is concluded that the ferroelectric instability is induced by rotation of O_6 octahedra, and the rotation of O_6 octahedra further give rise to the large displacements of La1 and Ti1. The major of spontaneous polarization of LTO is exactly come from the displacements of La1 and Til rather than the rotation of O_6 octahedra, where pure rotation of O_6 octahedra just gives a negative contribution for total polarization. Despite we conduct the analysis based on $Cmc2_1$ structure, the conclusion can also be applied on $P2_1$ structure where the origin of polarization is very similar to $Cmc2_1$ structure.

We conduct a lattice transformation to make the $Cmc2_1$ phase is compatible with the $P2_1$ unit cell, then the phase instability from $Cmc2_1$ to $P2_1$ structure can be studied against Γ-point distortions by computing the corresponding force-constant matrix $\boldsymbol{K}$. Two major negative eigenvalues associated to structural instability has been found, and the mode stiffness are computed by

$$\xi_m = \frac{\sum\limits_k M_k \omega_m^2 \gamma_{m,k}}{\sqrt{\sum\limits_k \gamma_{m,k}^2}}$$

(3)

where the m represents the mth phonon mode, M_k is the mass of kth atom in the unit cell, ω is the frequency of the phonon mode, and γ is the phonon eigendisplacements.

We labeled these two structural instabilities as ξ_1 and ξ_2. The values of computed mode stiffness for ξ_1 and ξ_2 are -3.45 and -4.70 eV/Å^2, respectively. The values are so strong that are obvious to represent the strong structural instability that can drive a phase transition from the $Cmc2_1$ to $P2_1$ phases, which supports that the $Cmc2_1$ structure is indeed the high-temperature ferroelectric phase. By checking the detailed individually atomic eigendisplacements, we found that displacement of oxygen amount to most of soft mode. The ξ_1 is major associated to in-phase tilting of O$_6$ octahedra around of in the rough [$01\bar{2}$] direction in $P2_1$ unit cell, where the O4 (they are still denoted in $Cmc2_1$ structure) captures the 50.1%, as well as O6 and O7 capture 34.8% of the norm of ξ_1. The ξ_2 is major associated to anti-phase tilting of O$_6$ octahedra around of in the rough [$01\bar{2}$] direction in $P2_1$ unit cell, where O4 captures 29.4%, as well as O5 and O7 capture 51.8% of the norm of ξ_2. All the La and Ti do not present significant eigendisplacements in the two structural instabilities. The structure from the deformation of $Cmc2_1$ phase has a = 7.792 Å, while $P2_1$ structure has a = 7.744 Å, it can be concluded that the lattice cannot resist the compressive stress with the decline of temperature, then the tilting of O$_6$ octahedra along a direction ensues to decrease the stress and therefore the phase transition from $Cmc2_1$ to $P2_1$ structure arise.
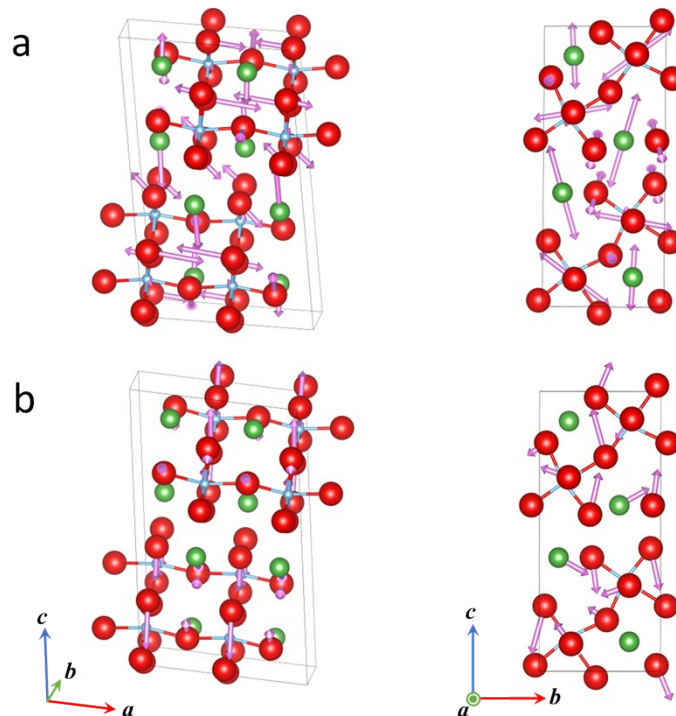
Figure S3 Displacement vectors of (a) S_1 mode and (b) Γ_1 mode. S1 mode always give the opposite displacement, hence, the contribution of net displacement is zero. Γ_1 mode can give a net displacement in *b* axis.

To understand the polarization change from $Cmc2_1$ to $P2_1$ structure, we conduct the symmetry mode analysis using AMPLIMODE software[7, 8] from the Bilbao Crystallographic Server[9] to gain insight into atomic displacement evolution. Three symmetry modes have been identified, Γ_1, Γ_2, and S_1, in which the S_1 is the most significant mode and captures 93.1% of total distortion, while Γ_1 captures 6.8% of total distortion and Γ_2 is negligible. The diagrams of the S1 and Γ1 mode are shown in Fig S3. Despite the S_1 is fairly strong to generate large displacement and induce the phase transition from $Cmc2_1$ to $P2_1$ structure, the symmetry of S_1 does not trigger net displacement for any one class of atom, that is, no any polarization change should be found. Hence, the decrease of polarization from $Cmc2_1$ to $P2_1$ structure should be contributed to the Γ_1 mode. Using equation (1), we find that the Γ_1 mode gives rise to a change in polarization of 0.082 C/m^2 along *b*-direction, which should be the origin of decreased polarization from $Cmc2_1$ to $P2_1$ phase transition. We identify La1 and Ti1 contribute to 67.8% and 19.1% in the polarization change, while total O atoms contributes to 20.8% (Ti2 contributes to -8.3%). The abnormal displacement of La1 should be closely related to S_1, where S_1 generates the mirror displacement (the center of La1 do not change) along polarization and hence makes the distance between displaced La1 and its adjacent O1 become smaller, then strong short-range repulsive interaction enforce La1 moves to the positive away from O1. The mirror displacement of La1 maybe is related to the shrinkage of lattice parameter *a*, making adjacent La1 is displaced to increase the distance between them and hence weakening the long-range Coulomb interaction. The Ti1 is also under the role of long-range Coulomb repulsion interaction, then the displacement change in the same direction with La1 is produced. Combined with the phase transition analysis, we can get a clear logical deduction to understand the origin of the abnormal polarization change from $Cmc2_1$ to $P2_1$ phase transition. The tilting of O$_6$ octahedra along *a* direction is the origin of phase instability,

and giving rise to the decline of lattice parameter a. Subsequently, the consequent Coulomb repulsion interaction between adjacent two La1 atoms make them produce mirror displacement to increase their distance. However, the mirror displacement of La1 shorten the distance between La1 and O1 and the strong short-range repulsion interaction between them enforce La1 moves toward the center of oxygen cage, which leads to the decrease of spontaneous polarization in $P2_1$ structure.

3. Piezoelectric Response Properties

Table S2 shows the computed piezoelectric stress tensor $e_{\alpha i}$ and piezoelectric strain tensor $d_{\alpha i}$ for the $P2_1$ phase of LTO. The computed piezoelectric responses are considerable but not particularly large. It can be found that the longitudinal piezoelectric constant d_{22} is the maximum of -13.54 pC/N, while the maximum shear piezoelectric constant is -4.48 pC/N. Hence, the fact of $|d_{22}/d_{16}|<1$ suggests that the LTO is the typical extender ferroelectrics,[10] that is, the maximum effective longitudinal piezoelectric constant is always found in the polarized direction. We plot the orientation dependence of effective d_{33}, as shown in Figure S2(e), which indicates that the maximum longitudinal piezoelectric constant can be found in b-direction. The piezoelectric constant d_{33} of poled polycrystal can be regarded as an orientational average of effective longitudinal piezoelectric constant in a certain area.[11] The magnitudes of these constants are determined by factors such as the material structure, composition, and lattice symmetry. Using the orientational average method, we can infer that the d_{33} of LTO ceramics is mainly derived from the d_{22} of LTO crystal. As for d_{22}, which represents the longitudinal polarization stretching under the external stress. It is noted that the $d_{22} = e_{21}s_{12} + e_{22}s_{22} + e_{23}s_{23} + e_{25}s_{25}$, where s_{ij} is the elastic compliance tensor and has been shown in Table S4. We can find that d_{22} is actually dominated by e_{22}. Recalling the definition of piezoelectric constant and equation (1), it is obtained

$$e_{22} = \left.\frac{\partial P_2}{\partial \eta_2}\right|_E \approx \frac{c}{\Omega}Z^*_{i,22}\left.\frac{\partial u_{i,2}}{\partial \eta_2}\right|_E$$

(4)

where η is strain, E is external electric field, c is the lattice parameter in polarization

direction and u is the internal atomic coordinate. The decomposed atomic contributions have been shown in Figure S2(f). It can be found that the atomic contributions for e_{22} broadly consistent with the contribution for polarization, in which the La1, La2, Ti1, Ti2, O9, O10, and O14 give the significant positive contribution in $P2_1$ structure. In addition, the group contained O1, O2, O3, and O4 give the negative contribution, being contrast to the group contained O5, O6, O7, and O8. The results are very similar to the situation of spontaneous polarization, which indicate the stronger rotation of O_6 octahedra after applied positive η_2. It must be noted that La1, La2, Ti1, and Ti2 contributes to about 70%, highlighting the importance of O_6 octahedra rotation at the edge of perovskite block. Unexpectedly, O9 and O10 also play a considerable role in e_{22}, suggesting that the interlayer in the perovskite block may follow the usual polarization stretching rule like the conventional perovskite ferroelectrics. Based on above understanding of e_{22}, it can be concluded that the piezoelectricity of LTO mainly comes from the La and Ti atoms near the outside of perovskite block, while the La and Ti atoms in the inside of perovskite block is almost unactivated.

Table S2. Calculated piezoelectric constants $e_{\alpha i}$ and $d_{\alpha i}$ (where i labels strain components in Voigt notation, given in C/m^2 and pC/N, respectively). The experimental values[12] are given in parenthesis.

e_{21}	-0.995	d_{21}	2.44 (6)
e_{22}	-3.177	d_{22}	-13.54 (16)
e_{23}	-0.187	d_{23}	2.95 (3)
e_{25}	0.084	d_{25}	-0.32
e_{14}	-0.082	d_{14}	-2.93
e_{16}	-0.051	d_{16}	-4.48
e_{34}	-0.045	d_{34}	-1.58
e_{36}	0.059	d_{36}	0.28

Table S3 Calculated dielectric tensors ϵ for monoclinic LTO, in unit of ϵ_0.

$$\epsilon = \begin{pmatrix} 72.56 & 0 & 0.85 \\ 0 & 50.89 & 0 \\ 0.85 & 0 & 39.87 \end{pmatrix}$$

Table S4 Calculated elastic tensors for monoclinic LTO, in unit of GPa for c, 10^{-12} m²/N for s.

$$c = \begin{pmatrix} 319.4 & 151.4 & 112.9 & 0 & -6.2 & 0 \\ 151.4 & 262.2 & 79.4 & 0 & -10.8 & 0 \\ 112.9 & 79.4 & 196.7 & 0 & -11.6 & 0 \\ 0 & 0 & 0 & 43.2 & 0 & -10.3 \\ -6.2 & -10.8 & -11.6 & 0 & 77.0 & 0 \\ 0 & 0 & 0 & -10.3 & 0 & 117.6 \end{pmatrix}$$

$$s = \begin{pmatrix} 4.86 & -2.24 & -1.90 & 0 & -0.21 & 0 \\ -2.24 & 5.39 & -0.86 & 0 & 0.44 & 0 \\ -1.90 & -0.86 & 6.57 & 0 & 0.71 & 0 \\ 0 & 0 & 0 & 23.63 & 0 & 2.08 \\ -0.21 & 0.44 & 0.71 & 0 & 13.14 & 0 \\ 0 & 0 & 0 & 2.08 & 0 & 8.68 \end{pmatrix}$$

Table S5 Calculated piezoelectric tensors for monoclinic LTO, in unit of C/m² for e, pC/N for d.

$$e = \begin{pmatrix} 0 & 0 & 0 & -0.082 & 0 & -0.510 \\ -0.995 & -3.177 & -0.187 & 0 & 0.084 & 0 \\ 0 & 0 & 0 & -0.045 & 0 & 0.059 \end{pmatrix}$$

$$d = \begin{pmatrix} 0 & 0 & 0 & -2.93 & 0 & -4.48 \\ 2.44 & -13.54 & 2.95 & 0 & -0.32 & 0 \\ 0 & 0 & 0 & -1.58 & 0 & 0.28 \end{pmatrix}$$

Experimental Study of LTO ceramics

The variation of crystal structural parameters and refined lattice parameters of the LTO-LC100*x* ceramics are shown in Figure S4 and Table S6. The lattice constants *b*, *c* and unit cell volume of Li/Ce modified LTO ceramics are increased slightly than those of pristine LTO. Due to the low doping content of Li/Ce and the and the radius of Ce ions is close to La ions, the doping did not cause significant changes in the lattice parameters.
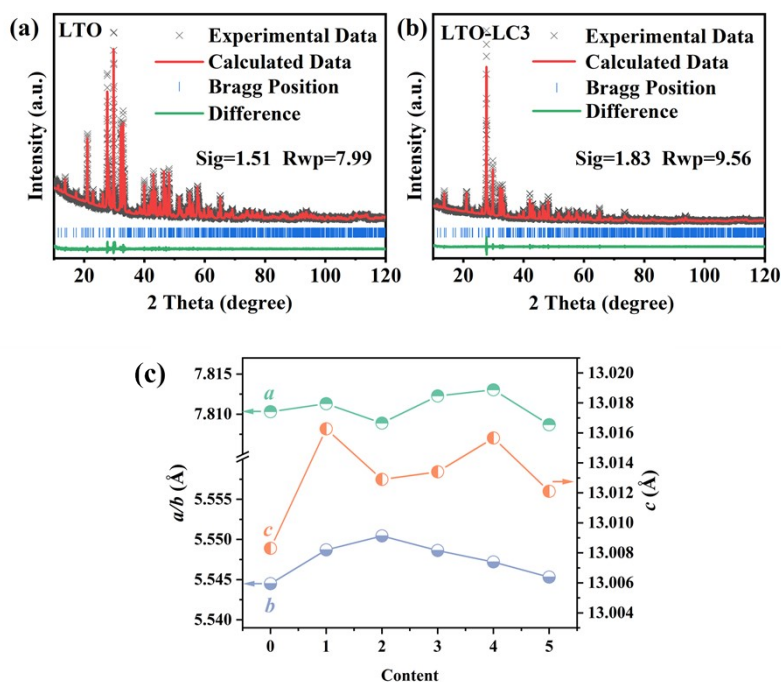

Figure S4 Rietveld refinement plots of (a) LTO and (b) LTO-LC3 ceramic powder. (c) variation of crystal structural parameters of the LTO-LC100*x* ceramics.

Table S6. Refined crystal structural parameters of ceramic samples.

Sample	a (Å)	b (Å)	c (Å)	β	Volume (Å³)
LTO	7.8103	5.5445	13.0083	98.6052	556.97
LTO-LC1	7.8113	5.5487	13.0163	98.6325	557.77
LTO-LC2	7.8089	5.5504	13.0129	98.6854	557.55
LTO-LC3	7.8123	5.5486	13.0134	98.5865	557.78

LTO-LC4	7.8130	5.5472	13.0157	98.6110	557.75
LTO-LC5	7.8087	5.5453	13.0121	98.6833	556.99

Table S7. Important Raman spectral band assignments of LTO ceramics.

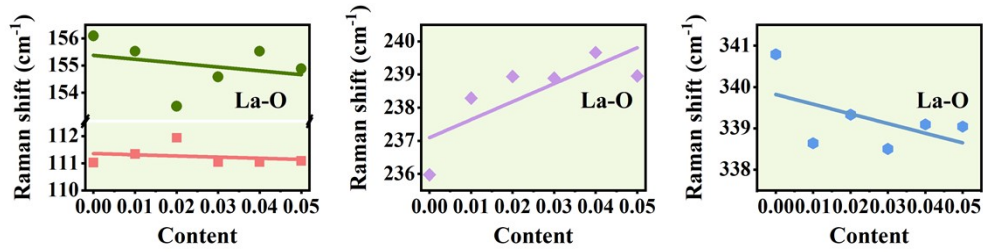| Raman shift (cm⁻¹)	Band assignment
111	La-O
152	La-O
239	La-O
339	La-O

Figure S5 The Li/Ce co-doping content dependence of Raman mode associated with La-O bonds in the $100 \sim 350$ cm⁻¹ region of LTO-LC100x ceramics

The point defects formation induced by Li/Ce dual doping as follows:

$$Li^+ \xrightarrow{\ La^{3+}\ } Li''_{La} + V_o^{\bullet\bullet} \tag{4}$$

$$Ce^{4+} \xrightarrow{\ La^{3+}\ } Ce^{\bullet}_{La} + e' \tag{5}$$
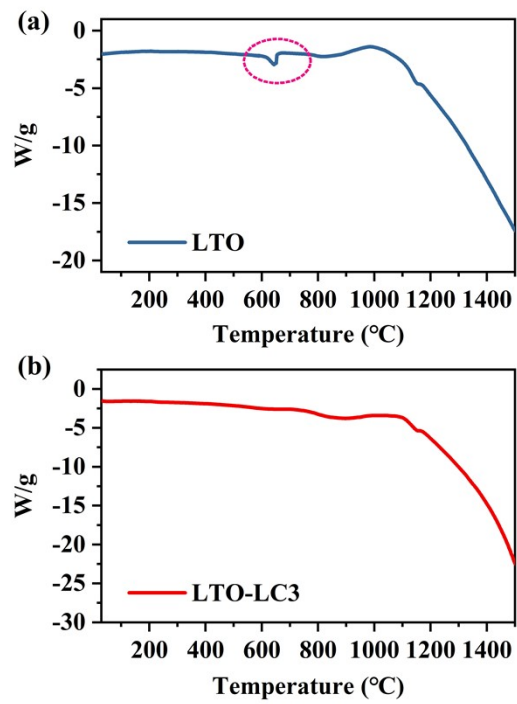
Figure S6 DSC curves of (a) LTO and (b) LTO-LC3. The valley of curve around 640 °C in LTO indicates the phase transition from $P2_1$ to $Cmc2_1$.
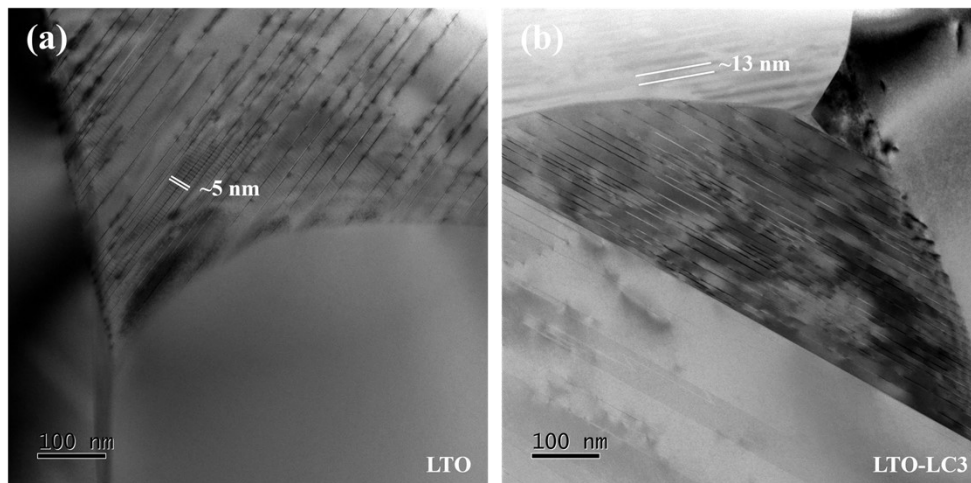

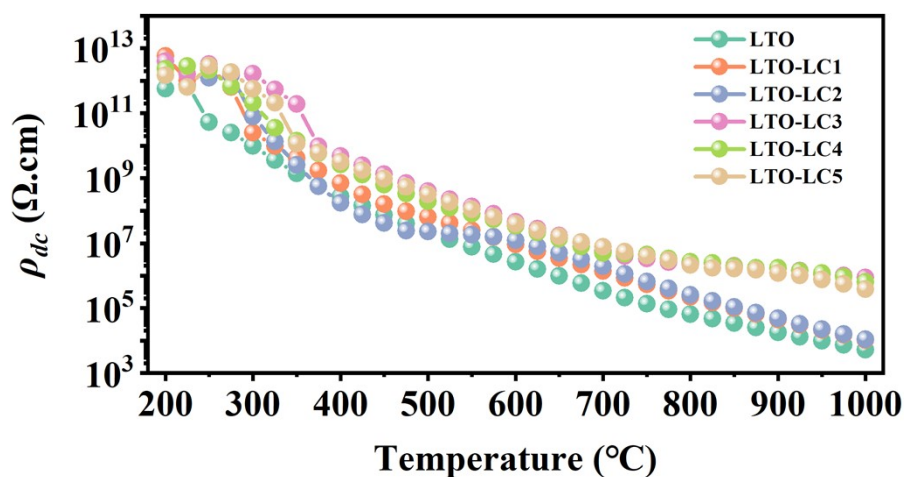**Figure S7** TEM image with domain structure of (a) LTO and (b) LTO-LC3.

Figure S8 The temperature dependent resistivity of LTO-LC100*x* ceramics.

The fitted complex impedance data of the LTO and LTO-LC3 ceramics at 700 °C displayed in Figure S9 and Table S8. The complex impedance diagram of LTO presents two very obvious semicircular arcs, representing the existence of gains and grain boundaries response. In contrast, the complex impedance spectrum of LTO-LC3 Exhibit only one semicircular arc, indicating the doped LTO ceramics are primarily controlled by grains response. From the impedance data obtained by fitting, the impedance of LTO-LC3 is obviously improved, further demonstrates that the Li/Ce dual doping can effectively increase the resistance.
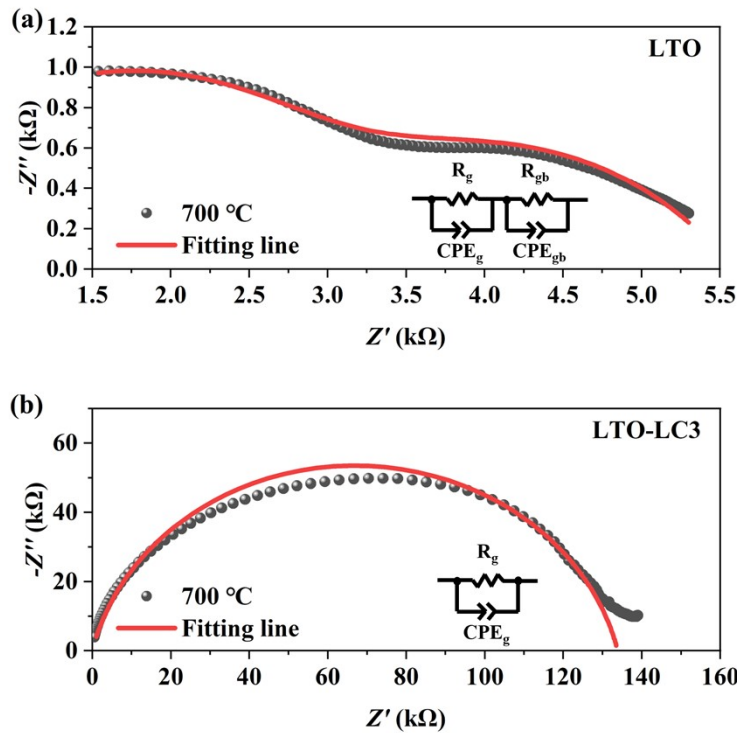
Figure S9 Fitted complex impedance spectrum of the (a) LTO and (d) LTO-LC3 ceramics at 700 °C.

Table S8. Fitted impedance data of LTO and LTO-LC3 ceramics

Sample	R_g (Ω)	R_{gb} (Ω)
LTO	2890	2697
LTO-LC3	133890	/

The normalized Z''/Z''_{max} plot can more clearly show the contribution of grains and grain boundaries to the conductance of ceramic samples. As shown in Figure 10(a), the peak in the low frequency region represents the grain boundary conductance, and the peak in the high frequency region represents the grain conductance.[13] However, there is only one single peak in the high frequency region in the LTO-LC3 diagram, which indicates that Li/Ce dual doping has an inhibitory effect on the grain boundary conductance. The frequency dependence of normalized electrical modulus M''/M''_{max} of

LTO and LTO-LC3 ceramics is shown in Figure S10(b). The movement trend of M''/M''_{max} peaks in LTO-LC3 is consistent with the Z''/Z''_{max} peaks, indicating the existence of thermal activation relaxation or dipole reorientation in ceramic samples.[14, 15]
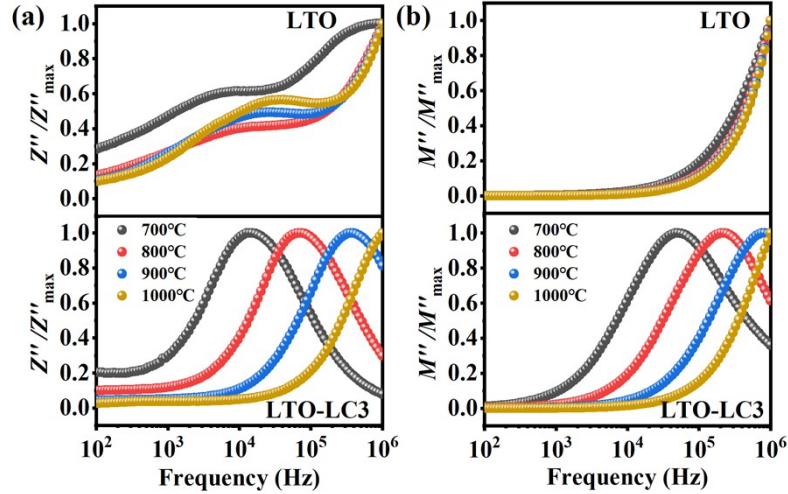

Figure S10 (a) Frequency dependence of normalized impedance Z''/Z''_{max} of LTO and LTO-LC3 ceramics. (b) Frequency dependence of normalized electrical modulus M''/M''_{max} of LTO and LTO-LC3 ceramics.

The tanδ-T curves of LTO and LTO-LC3 ceramics in different frequency are shown in Figure S11. As the temperature rises, the tan δ values of both ceramic materials increase accordingly, indicating the presence of thermal activation conduction phenomena. In the high-temperature region, the significant increase in tanδ values may be attributed to the charge carriers gaining higher energy due to the temperature rise, thus making it easier to overcome potential barriers and participate in the conduction process. The tan δ values of LTO-LC3 are generally lower than those of LTO at the same frequency. This is because the doping has optimized the structure and composition, making it more difficult to activate the charge carriers at high temperatures. As a result, the LTO-LC3 material exhibits better thermal stability and lower energy dissipation over the entire temperature range.
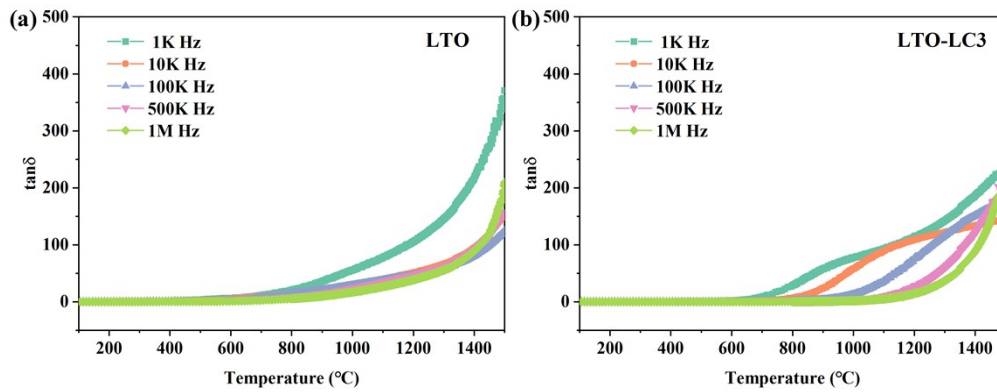
Figure S11 The tanδ-T curves of (a) LTO and (b) LTO-LC3 ceramics in different frequency.

Calculation Details

The first-principle calculations in the present work are carried out using Vienna Ab initio Simulation Package (VASP) based on density functional theory (DFT)[16, 17]. The PBEsol [18] exchange-correlation functional with projector-augmented wave (PAW) [19] is employed in the calculations. The La $5s^25p^66s^25d^1$, Ti $3s^23p^64s^23d^2$, and O $2s^22p^4$ states are treated as valence electrons for calculations. The wave function is represented as a plane wave expansion that is truncated at a cut-off energy of 520 eV. Γ-centered k-point meshes with a grid of spacing $0.04 \times 2\pi$ Å^{-1} for Brillouin zone sampling were chosen. The macroscopic polarization of LTO is defined by the so-called modern theory of polarization using the Berry phase method [20]. The force-constant matrix, dielectric, elastic and piezoelectric tensors as the second derivatives of total internal energy are extracted by density functional perturbation theory (DFPT) [21] and finite differences method.

References

1.   J. López-Pérez and J. Iñiguez, *Phys. Rev. B*, 2011, **84**, 13.

2.   N. Ishizawa, F. Marumo, S. Iwai, M. Kimura and T. Kawamura, *Acta Crystallogr. B*,

1982, **38**, 368-372.

3.   M. Gasperin, *Acta Crystallogr. B*, 1975, **31**, 2129-2130.

4.   E. Bruyer and A. Sayede, *J. Appl. Phys.*, 2010, **108**, 9.

5.   T. Gu, T. Scarbrough, Y. R. Yang, J. Iniguez, L. Bellaiche and H. J. Xiang, *Phys. Rev. Lett.*, 2018, **120**, 6.

6.   Y. B. Zhang, J. W. Sun, J. P. Perdew and X. F. Wu, *Phys. Rev. B*, 2017, **96**, 16.

7.   J. M. Perez-Mato, D. Orobengoa and M. I. Aroyo, *Acta Crystallographica a-Foundation and Advances*, 2010, **66**, 558-590.

8.   D. Orobengoa, C. Capillas, M. I. Aroyo and J. M. Perez-Mato, *J. Appl. Crystallogr.*, 2009, **42**, 820-833.

9.   M. I. Aroyo, J. M. Perez-Mato, D. Orobengoa, E. Tasci, G. de la Flor and A. Kirov, *Bulg. Chem. Commun.*, 2011, **43**, 183-197.

10.   M. Davis, M. Budimir, D. Damjanovic and N. Setter, *J. Appl. Phys.*, 2007, **101**, 10.

11.   Z. Tan, J. W. Xi, J. Xing, B. Wu, Q. M. Zhang, Q. Chen and J. G. Zhu, *J. Eur. Ceram. Soc.*, 2022, **42**, 3865-3876.

12.   S. Nanamatsu, M. Kimura, K. Doi, S. Matsushita and N. Yamada, *Ferroelectrics*, 1973, **8**, 511-513.

13.   Y. Y. Li, L. M. Jiang, C. Wu, Z. C. Liu, X. J. Zhao, Q. Chen, J. Xing and J. G. Zhu, *Ceram. Int.*, 2019, **45**, 12742-12756.

14.   C. C. Wang, J. Wang, X. H. Sun, L. N. Liu, J. Zhang, J. Zheng and C. Cheng, *Solid State Commun.*, 2014, **179**, 29-33.

15.   O. Raymond, R. Font, J. Portelles, N. Suárez-Almodovar and J. M. Siqueiros, *J.*

Appl. Phys., 2006, **99**, 9.

16. G. Kresse and J. Hafner, *Phys. Rev. B*, 1994, **49**, 14251-14269.

17. G. Kresse and J. Furthmuller, *Phys. Rev. B*, 1996, **54**, 11169-11186.

18. J. P. Perdew, A. Ruzsinszky, G. I. Csonka, O. A. Vydrov, G. E. Scuseria, L. A. Constantin, X. L. Zhou and K. Burke, *Phys. Rev. Lett.*, 2008, **100**, 4.

19. P. E. Blochl, *Phys. Rev. B*, 1994, **50**, 17953-17979.

20. R. D. Kingsmith and D. Vanderbilt, *Phys. Rev. B*, 1993, **47**, 1651-1654.

21. X. Wu, D. Vanderbilt and D. R. Hamann, *Phys. Rev. B*, 2005, **72**, 13.